arXiv:1702.04793v2 [cond-mat.supr-con] 26 Feb 2017

Controlling competing orders *via* non-equilibrium acoustic phonons: emergence of anisotropic electronic temperature

Michael Schütt,[1] Peter P. Orth,[2] Alex Levchenko,[3] and Rafael M. Fernandes[1]

[1] *School of Physics and Astronomy, University of Minnesota, Minneapolis, Minnesota 55455, USA*
[2] *Department of Physics and Astronomy, Iowa State University, Ames, Iowa 50011, USA*
[3] *Department of Physics, University of Wisconsin-Madison, Madison, Wisconsin 53706, USA*

(Dated: February 28, 2017)

Ultrafast perturbations offer a unique tool to manipulate correlated systems due to their ability to promote transient behaviors with no equilibrium counterpart. A widely employed strategy is the excitation of coherent optical phonons, as they can cause significant changes in the electronic structure and interactions on short time scales. Here, we explore a promising alternative route: the non-equilibrium excitation of acoustic phonons. We demonstrate that it leads to the remarkable phenomenon of a momentum-dependent temperature, by which electronic states at different regions of the Fermi surface are subject to distinct local temperatures. Such an anisotropic electronic temperature can have a profound effect on the delicate balance between competing ordered states in unconventional superconductors, opening a novel avenue to control correlated phases.

Introduction – One of the hallmarks of correlated electronic systems, epitomized in the phase diagrams of unconventional superconductors, is the existence of multiple electronic orders with comparable energy scales that entangle different degrees of freedom. The standard ways to experimentally tune these phases is by chemical substitution, pressure, or magnetic field. Recent advances in ultrafast pump-and-probe techniques, however, opened a new avenue to explore and control different types of electronic orders, as they generally respond differently to dynamic perturbations [1–9]. Importantly, by taking the system out of equilibrium, the system parameters change on ultrafast time scales, which can result in transient electronic states not present in equilibrium. An earlier experimental demonstration of non-equilibrium control of electronic order, based on pioneering ideas by Eliashberg [10, 11], was the surprising enhancement of superconductivity by sub-gap microwave irradiation [12]. More recently, ultrafast optical pulses have been used to select particular lattice excitations of correlated systems by matching the pulse frequency to that of optical phonon modes [13]. These coherent lattice excitations then modify the electronic structure and interactions of the system, which can for instance favor superconductivity over other competing electronic ordered states – a concept widely explored theoretically [14–24]. Examples include the melting of stripe order in the cuprates [4], the coherent modulation of the chemical potential in the pnictides [5], and the possible promotion of transient superconductivity at high temperatures in organic superconductors [8]. The fact that the transient light-induced states only exist on ultrashort few picosecond time scales, however, poses a key challenge to stabilize non-equilibrium states of matter for longer times.

Here we show that the non-equilibrium excitation of *acoustic phonons* provides a promising framework to manipulate correlated electronic phases on long time scales. Although acoustic phonons do not couple directly to light, they can be excited by rapidly applying lattice strain via an interface or piezoelectric devices [3, 25–27]. The main difference with respect to optical phonons is that scattering of electrons by acoustic phonons can provide significant momentum transfer with little energy absorption. Importantly, while optical phonon modes are usually isotropic, acoustic phonons are intrinsically anisotropic. As a result, the coupling between the electronic subsystem and the non-equilibrium distribution of acoustic phonons leads to a redistribution of electronic quasiparticles close to the Fermi surface without generating too much heating. As we show below, this redistribution of electronic spectral weight is then translated into an *anisotropic electronic temperature profile* $\delta T_{\mathbf{p}}$ on the Fermi surface, resulting in momentum-selective heating of the low-energy electronic states (see Fig. 1a).

Our calculations reveal that the precise shape of the temperature profile $\delta T_{\mathbf{p}}$ can be tuned by selecting the energy of the excited acoustic phonons. Furthermore, because the anisotropy of $\delta T_{\mathbf{p}}$ is a consequence of the anisotropy of the phonon velocity, the effect discovered here is amplified near a structural phase transition, where the phonon velocity is strongly suppressed along particular directions. This feature makes unconventional superconductors – iron pnictides, cuprates, and heavy fermions – promising systems to be manipulated by non-equilibrium acoustic phonons, since some of their phase diagrams display large nematic fluctuations, which cause strong lattice softening [28, 29].

What is the relevance of such a long-lived steady state with a momentum-dependent temperature profile? Because this state is fundamentally different from any equilibrium state, it opens an unexplored path to probe and control correlated phases. More specifically, in the context of unconventional superconductors, properly tuning the anisotropy of the temperature profile allows one to selectively melt the various density-wave types of order that are known to compete with superconductivity, thus potentially enhancing the superconducting transiton temperature T_c. Indeed, while in the iron pnictides s^{+-} su-

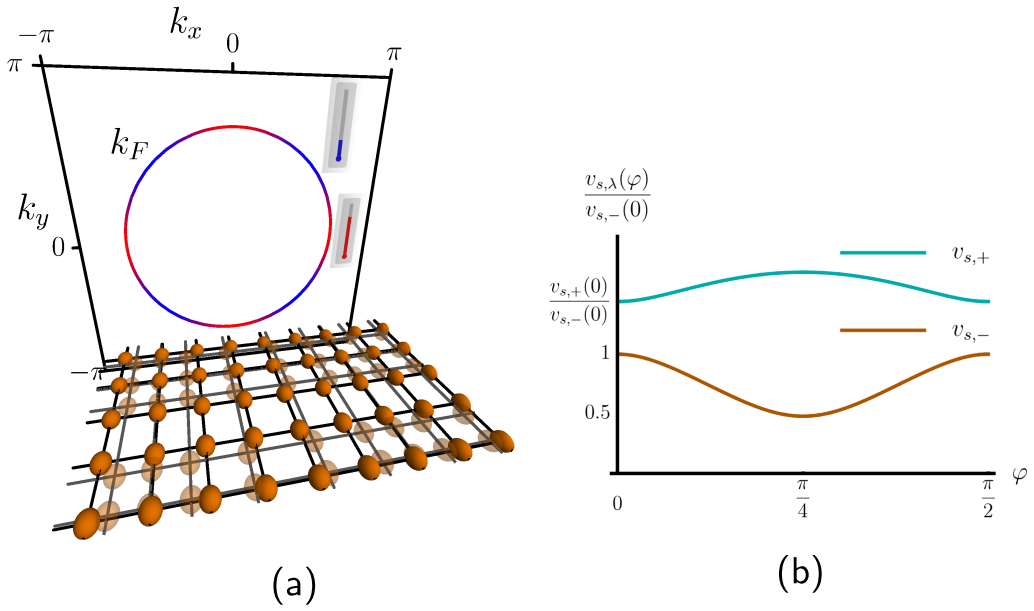

FIG. 1. **Momentum-dependent electronic temperature generated by non-equilibrium acoustic phonons**. (a) The lower panel illustrates the instantaneous distortions on a square lattice caused by the excitation of an acoustic phonon mode. The solid (semi-transparent) lines and symbols refer to the undistorted (distorted) lattice. Scattering by non-equilibrium acoustic phonons promotes a momentum-dependent redistribution of electronic quasi-particles, which is translated as a steady-state temperature profile that varies along the Fermi surface, depicted in the upper panel (blue and red represent local temperatures that are colder and hotter than the average, respectively). (b) Anisotropic sound velocity $v_{s,\lambda}$ of the two in-plane acoustic phonon modes as a function of the propagation direction φ. In this and in the next figures, we set the ratio $(C_{11}-C_{12})/(2C_{66}) = 1/4$.

perconductivity competes with a spin density-wave order with ordering vector $\mathbf{Q} = (\pi, 0)$ [30], in the cuprates the d-wave superconducting T_c is suppressed by the onset of incommensurate charge order with wave-vector $\mathbf{Q} \approx \left(\frac{\pi}{3a}, 0\right)$ [31]. Similarly, the superconducting state of the heavy fermions competes with a Néel-type magnetic order characterized by $\mathbf{Q} = (\pi, \pi)$ [32]. These competing density-wave instabilities are mostly affected by particular points of the Fermi surface called "hot spots" – pairs of points connected by the ordering vector $\mathbf{Q}$. In contrast, the superconducting instability is affected by most low-energy electronic states. As a result, when the local temperature of these hot spots is larger than the average temperature across the entire Fermi surface, the competing density-wave instability is suppressed, and superconductivity can be enhanced. We demonstrate this very general effect below by explicitly calculating the steady-state phase diagram of a low-energy model widely employed to study competing superconducting and spin-density wave order in the iron pnictides.

Microscopic model – Our starting point is the electron-phonon Hamiltonian $H = H_{\rm el} + H_{\rm ph} + H_{\rm el-ph}$. Here, $H_{\rm el}$ describes an interacting electronic system $H_{\rm el} = H_0 + H_{\rm int}$ with kinetic term $H_0 = \sum_{\mathbf{p}} \xi_{\mathbf{p}} c^\dagger_{\mathbf{p},\sigma} c_{\mathbf{p},\sigma}$, where the operator $c^\dagger_{\mathbf{p},\sigma}$ creates an electron with momentum $\mathbf{p}$ and spin σ and $\xi_{\mathbf{p}}$ is the band dispersion. The interaction term $H_{\rm int}$ is responsible for the superconducting and density-wave instabilities of the system. The phonons are described by the harmonic term $H_{\rm ph} = \sum_{\mathbf{q},\lambda} \omega_{\mathbf{q},\lambda} a^\dagger_{\mathbf{q},\lambda} a_{\mathbf{q},\lambda}$, where the operator $a^\dagger_{\mathbf{q},\lambda}$ creates a phonon with momentum $\mathbf{q}$ and energy $\omega_{\mathbf{q},\lambda}$ in branch λ. In the long wavelength regime, $\omega_{\mathbf{q},\lambda} = v_{s,\lambda}(\varphi_{\mathbf{q}})|\mathbf{q}|$, where we introduced the sound velocity $v_{s,\lambda}$, which depends on the propagation direction $\varphi_{\mathbf{q}} \equiv \tan^{-1}(q_y/q_x)$. Finally, the electron-phonon term is:

$$H_{\rm el-ph} = \sum_{\substack{\mathbf{p},\mathbf{p}',\mathbf{q} \\ \mathbf{G},\lambda,\sigma}} \left(M_{\mathbf{p},\mathbf{p}',\mathbf{q},\lambda}\, a^\dagger_{\mathbf{q},\lambda} c^\dagger_{\mathbf{p},\sigma} c_{\mathbf{p}',\sigma} \delta_{\mathbf{p}'-\mathbf{p}-\mathbf{q}+\mathbf{G}} + \text{h.c.} \right) \tag{1}$$

with momentum conserved up to a reciprocal lattice vector $\mathbf{G}$. The matrix element $M_{\mathbf{p},\mathbf{p}',\mathbf{q},\lambda}$ is typically approximated, in the long wavelength regime, by

$$|M_{\mathbf{p}-\mathbf{p}'=\mathbf{q},\lambda}|^2 \propto \frac{(\mathbf{q}\cdot\mathbf{e}_{\mathbf{q},\lambda})^2}{v_{s,\lambda}(\varphi_{\mathbf{q}})|\mathbf{q}|} \tag{2}$$

with transferred momentum $\mathbf{q}$ and phonon polarization $\mathbf{e}_{\mathbf{q},\lambda}$. The polarization and dispersion of the acoustic phonon modes are determined solely by the properties of the elastic tensor. Since many of our systems of interest are tetragonal and layered, we consider here the case of a square lattice, which has two phonon branches [33]:

$$v_{s,\pm}(\varphi_{\mathbf{q}}) = \frac{1}{\sqrt{2\rho}} \sqrt{\mu_1 \pm \sqrt{\frac{\mu_2^2+\mu_3^2}{2} + \frac{(\mu_2^2-\mu_3^2)\cos 4\varphi_{\mathbf{q}}}{2}}} \tag{3}$$

Here, ρ is the density and the μ_i coefficients are related to the elastic constants C_{ij} via $\mu_1 = C_{11} + C_{66}$, $\mu_2 = C_{11} - C_{66}$ and $\mu_3 = C_{12} + C_{66}$. Hereafter, we focus our analysis only on the low-energy phonon mode, $\omega_{\mathbf{q},-}$, and drop the branch index λ. The anisotropy of this mode, which is four-fold symmetric, depends on the relative strength of the elastic constants, since $\frac{v_s(0)}{v_s(\pi/4)} = \sqrt{\frac{2C_{66}}{C_{11}-C_{12}}}$. As a result, the phonon anisotropy is stronger in systems close to a tetragonal-to-orthorhombic lattice instability, since in this case either $C_{66} \to 0$ (corresponding to a B_{2g} xy deformation of the square lattice) or $C_{11}-C_{12} \to 0$ (corresponding to a B_{1g} x^2-y^2deformation of the square lattice). Because the phase diagrams of the iron pnictides, of some cuprates, and of some heavy fermions display nematic fluctuations [28, 29] related to a B_{1g} tetragonal-to-orthorhombic instability, we focus on the case $(C_{11} - C_{12})/2 \ll C_{66}$. In this situation, the sound velocity is minimum at $\varphi = \pi/4$ and maximum at $\varphi = 0$, as shown in Fig. 1b.

The polarization $\mathbf{e}_{\mathbf{q},-}$ of the low-energy phonon mode described by Eq. (3) turns out to be almost transversal for all values of $\mathbf{q}$, resulting in a nearly vanishing matrix element $M_{\mathbf{q},-}$ according to Eq. (2). Thus, one has to consider umklapp processes where $\mathbf{q}$ is conserved up to a reciprocal lattice vector $\mathbf{G} \neq 0$. As shown in the supplementary material (SM), the dominant umklapp contribution gives $|M_{q,\varphi}|^2 \propto \frac{q}{v_s(\varphi)}$, which we adopt hereafter. This expression highlights that an anisotropy in the sound velocity results in an anisotropic electron-phonon interaction.

Phonon-induced redistribution of electronic quasi-particles – Having established the properties of the coupling between electrons and phonons, we now discuss how driving the acoustic phonons out of equilibrium affects the low-energy electronic states. Experimentally, a non-equilibrium distribution of acoustic phonons, which we denote by $n_B(\omega_{\mathbf{q}})$, can be generated by propagation of shock waves through interfaces [2, 3, 25–27, 34]. Theoretically, the separation between electronic and phononic time scales within the Born-Oppenheimer approach allows for a quasi-classical treatment of the problem, in which out-of-equilibrium phonons inelastically scatter electronic quasi-particles between their momentum eigenstates. The resulting electronic distribution function $n^F_{\xi_{\mathbf{p}}}$ is then given by the solution of the Boltzmann equation $I^{\text{phonon}}_{\text{coll}}[n^F, n^B] = 0$, where $I^{\text{phonon}}_{\text{coll}}$ denotes the phonon collision kernel:

$$I^{\text{phonon}}_{\text{coll}}[n^F, n^B] = -\sum_{\alpha=\pm} \alpha \int \frac{\mathrm{d}^2 p'}{(2\pi)^2} \delta(\xi_{\mathbf{p}} - \xi_{\mathbf{p}'} - \alpha\omega_{\mathbf{p}-\mathbf{p}'}) |M_{\mathbf{p}-\mathbf{p}'}|^2 \left[n^F_{\xi_{\mathbf{p}}} n^F_{-\xi_{\mathbf{p}'}} n^B_{-\alpha\omega_{\mathbf{p}-\mathbf{p}'}} + n^F_{-\xi_{\mathbf{p}}} n^F_{\xi_{\mathbf{p}'}} n^B_{\alpha\omega_{\mathbf{p}-\mathbf{p}'}} \right], \quad (4)$$

Here, we introduced the convention $n^F_{-x} = 1 - n^F_x$ and $-n^B_{-x} = n^B_x + 1$. The physical meaning of the Boltzmann equation is clear: in order for the system to maintain a homogeneous quasi-particle distribution in the steady-state, any deviation of the phonon distribution function from the Bose-Einstein function n^B_0 must be compensated by a deviation of the electronic distribution from the Fermi function n^F_0 – provided, of course, that no other faster relaxation process occurs, a condition that is satisfied by several systems [35]. To focus on the general properties of the mechanism proposed here, we consider small deviations from equilibrium, $n^{F/B}_{\mathbf{p}} = n^{F/B}_{0,\mathbf{p}} - (\partial_{\xi_{\mathbf{p}}} n^{F/B}_{0,\mathbf{p}}) h^{F/B}_{\mathbf{p}}$, and solve the linearized Boltzmann equation to determine the electronic non-equilibrium distribution function h^F for a given phononic distribution function h^B (details in the SM).

While the equilibrium electronic distribution $n^F_{0,\mathbf{p}}$ is determined entirely by the chemical potential μ and the temperature T, the out-of-equilibrium distribution can generally be parametrized in terms of a momentum-dependent effective temperature $T+\delta T_{\hat{\mathbf{p}}}$, with $\hat{\mathbf{p}} = \mathbf{p}/|\mathbf{p}|$, and effective chemical potential $\mu + \delta\mu_{\hat{\mathbf{p}}}$, i.e. $h^F_{\mathbf{p}} = \delta\mu_{\hat{\mathbf{p}}} + \frac{\xi_{\mathbf{p}}}{T}\,\delta T_{\hat{\mathbf{p}}}$. Such a parametrization is particularly useful for the states near the Fermi level, where the energy scales associated with momenta perpendicular and parallel to the Fermi surface are very different. In our problem, because the interaction with a single acoustic phonon cannot modify the chemical potential locally, $\delta\mu_{\hat{\mathbf{p}}}$ is zero. Furthermore, the small energy transfer resulting from the electron-phonon scattering constrains the low-energy electrons to remain near the Fermi surface. As a result, the steady-state non-equilibrium electronic distribution function is completely encoded in the momentum-dependent temperature $\delta T_{\hat{\mathbf{p}}}$. Note that this approximation is valid for a non-current-carrying state, otherwise an additional shift of the momentum states would be required.

The precise momentum dependence of the effective electronic temperature $\delta T_{\hat{\mathbf{p}}}$ depends on the type of phonon distribution function h^B. As expected, in the simple case of a uniform heating of the phonons, the solution of the Boltzmann equation gives a momentum-independent electronic temperature shift. In order to induce anisotropies in $\delta T_{\hat{\mathbf{p}}}$, it is sufficient to excite phonons around a well-defined energy ω_0, as the geometrical constraints imposed by momentum and energy conservations, together with the anisotropy of the sound velocity, cause an anisotropic redistribution of quasi-particles. While the controlled excitation of a non-thermal acoustic

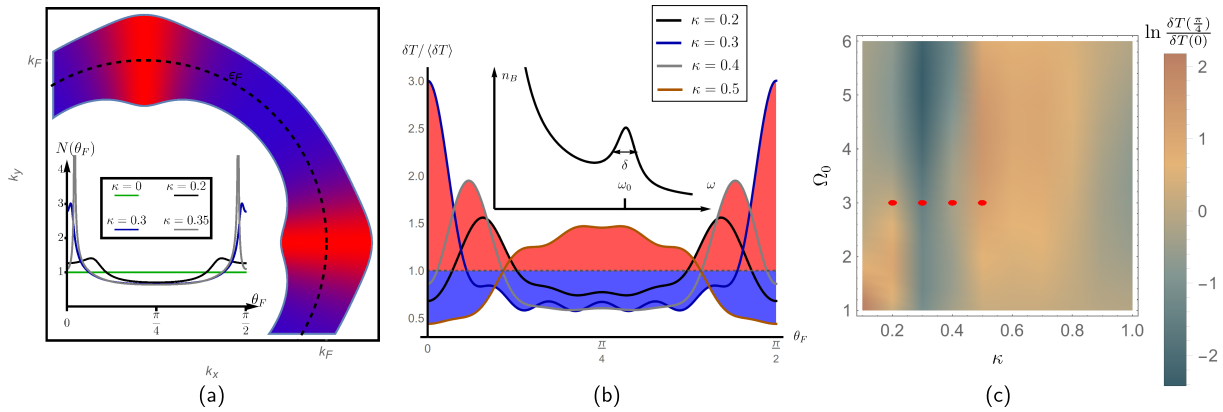

FIG. 2. **Anisotropic redistribution of electronic state and non-uniform heating of the Fermi surface states.** (a) Due to the geometric constraint imposed by momentum conservation, Eq. (5), the electronic states capable of absorbing acoustic phonons are not uniformly distributed around the Fermi surface (black dashed line). States near the red thick (blue thin) regions have a larger (smaller) phase space for phonon scattering. The inset shows the density of electronic states $N(\theta_F)$ available for the scattering of an electron at a Fermi surface angle θ_F by a phonon of energy ω_0, for different values of the dimensionless parameter $\kappa \equiv \left(\frac{\omega_0}{2\varepsilon_F}\right)/\left(\frac{v_s(0)}{v_F}\right)$. (b) Momentum-dependent temperature profile $\delta T(\theta_F)$, normalized by the average heating $\langle\delta T\rangle$, for different values of κ. The phonon non-equilibrium distribution n_B is depicted in the inset. We set the ratio $\Omega_0 \equiv \omega_0/2T = 3$. Due to the scattering of electrons by non-equilibrium phonons, certain regions of the Fermi surface are locally hotter (red shade) or colder (blue shade) than the average. The typical momenta associated with the hot/cold regions change as function of κ. (c) Color plot of the anisotropy of the non-uniform temperature, as defined by the logarithm of the ratio $\delta T(\pi/4)/\delta T(0)$, as function of the two dimensionless parameters κ and Ω_0. Blue (yellow) denotes dominant heating near $\theta_F = 0, \pi/2$ ($\theta_F = \pi/4$). The red symbols correspond to the curves shown in panel (b).

phonon population remains an experimental challenge, advances in the transmission of shock waves via interfaces and in the application of time-dependent strain via piezoelectrics provide promising prospects [26, 34].

To illustrate this generic effect, we consider a circular Fermi surface of radius p_F, as shown in Fig. 2a. In this case, the momenta parallel to the Fermi surface are labeled by the polar angle θ_F (measured with respect to the p_x axis). Momentum conservation enforces a relationship between the initial momentum θ_F and the final momentum θ'_F, $q = 2p_F \sin\left(\frac{\theta_F - \theta'_F}{2}\right)$, where q is the phonon momentum. Now, the phonon has a well-defined energy, $q = \omega_0/v_s(\varphi_{\mathbf{q}})$, and a well-defined propagation direction $\varphi_{\mathbf{q}}$, which is also related to the initial and final momenta, $2\varphi_{\mathbf{q}} = \pi + \theta_F + \theta'_F$. As a result, for a given momentum θ_F, the allowed values for θ'_F are given by the solution of the implicit equation:

$$\kappa = \tilde{v}_s\left(\frac{\theta_F + \theta'_F}{2}\right)\sin\left(\frac{\theta_F - \theta'_F}{2}\right) \qquad (5)$$

where we introduced the dimensionless parameter $\kappa \equiv \left(\frac{\omega_0}{2\varepsilon_F}\right)/\left(\frac{v_s(0)}{v_F}\right)$ relating the typical sound velocity $v_s(0)$, the Fermi velocity v_F, the excited phonon frequency ω_0, and the Fermi energy ε_F. The normalized phonon velocity, $\tilde{v}_s(\varphi) \equiv v_s(\varphi)/v_s(0)$, is by definition always smaller than 1, since the sound velocity is maximum at $\varphi = 0$. The key point of Eq. (5) is that the parameter κ strongly affects the allowed values for the pair of momenta (θ_F, θ'_F). For example, when $\kappa \ll 1$ the solution of Eq. (5) requires the initial and final momenta to be very close, $\theta'_F \approx \theta_F$, whereas when $\kappa > \frac{v_s(\pi/4)}{v_s(0)}$, there is no pair of momenta (θ_F, θ'_F) that solves Eq. (5). Note the key role played by the anisotropy in the sound velocity $\tilde{v}_s\left(\frac{\theta_F + \theta'_F}{2}\right)$: without it, the equation would only depend on the relative momentum $\theta_F - \theta'_F$.

For intermediate values of κ, the geometric constraint imposed by Eq. (5) implies that the electronic states that can absorb an acoustic phonon are not equally distributed around the Fermi surface. To quantify this important property, we use Eq. (5) to compute the density of available states, $N(\theta_F)$, for an electron with momentum θ_F scattered by a phonon of energy ω_0. In Fig. 2a, we show the behavior of $N(\theta_F)$ projected along the Fermi surface for $\kappa = 0.3$: it is clear that Fermi surface states with $\theta_F = 0, \pi/2$ are much more efficient in absorbing the acoustic phonons as compared to the states with $\theta_F = \pi/4$. Consequently, the effective temperature along $\theta_F = \pi/4$, as caused by phonon scattering, will generally be smaller than along $\theta_F = 0, \pi/2$. This is the microscopic origin of the momentum-dependent temperature induced by non-equilibrium acoustic phonons. Note from the inset of Fig. 2a that the region of the Fermi surface that is more affected by phonon scattering changes continuously as function of κ, becoming narrower as κ approaches the limiting value $\frac{v_s(\pi/4)}{v_s(0)} \approx 0.5 < 1$. Consequently, the degree of anisotropy in the effective temperature is controlled by the energy of the excited

phonons ω_0. Since $\kappa \sim \mathcal{O}(1)$, the relevant phonon energies are always much smaller than the Fermi energy, $\omega_0/\varepsilon_F \sim \mathcal{O}(v_s(0)/v_F)$.

Momentum-dependent temperature – The analysis above is confirmed by explicit solution of the Boltzmann equation for $\delta T_{\mathbf{p}}$. In the case of phonons excited near an energy ω_0, the non-equilibrium bosonic distribution function is modeled as (see the inset in Fig. 2b):

$$h^B_{\mathbf{q}} = W_B \, \frac{\delta}{\delta^2 + \left(\frac{\omega_{\mathbf{q}}}{2T} - \Omega_0\right)^2} \, . \tag{6}$$

Here, the parameter $\delta \ll 1$ represents the energy width of the excited phonons, W_B is an overall amplitude corresponding to the number of bosons excited by the external drive, and $\Omega_0 \equiv \frac{\omega_0}{2T}$. In Fig. 2b, we show the momentum-dependent temperature profiles $\delta T(\theta_F)$ obtained by solving the Boltzmann equation for a fixed Ω_0 as function of the parameter κ. For small values of κ, the anisotropy (as measured by the ratio $\delta T(\frac{\pi}{4})/\delta T(0)$) is mild, and the states with momentum $\theta_F = \pi/4$ are hotter than those with momenta $\theta_F = 0, \pi/2$. Upon increasing κ, the anisotropy is not only reversed, but also increased – in particular, the maximum anisotropy takes place for $\kappa \approx 0.3$, when the $\theta_F = 0, \pi/2$ states are the hottest states at the Fermi surface. Upon further increasing κ, the hottest region of the Fermi surface moves back towards the diagonal, but the amplitude of the anisotropy decreases. Remarkably, the changes in $\delta T(\theta_F)$ as function of κ are nearly insensitive to the value of Ω_0, as shown in Fig. 2c.

This behavior of $\delta T(\theta_F)$ is in qualitative agreement with the geometrical analysis of Fig. 2a, which shows that the largest density of electronic states capable of absorbing a phonon moves from the Fermi surface region near $\theta_F = \pi/4$ to $\theta_F = 0, \pi/2$ and then back to $\theta_F = \pi/4$ as κ increases. The fact that the amplitude of the anisotropy is not monotonic can be attributed to the fact that the maximum of the density $N(\theta_F)$ becomes not only larger but also narrower as κ increases, while the distribution function (6) is sensitive to a window of energies centered around ω_0.

Impact on competing electronic phases – The fact that electrons interacting with a non-equilibrium distribution of acoustic phonons are subject to a momentum-dependent temperature can be used as a tool to control and manipulate competing electronic states in correlated systems. The idea is that, by tuning the excited phonon energy ω_0 (proportional to the parameter κ discussed above), one can in principle selectively heat certain regions of the Fermi surface. While applicable to any form of non-isotropic order, this is particularly relevant for density-wave instabilities, which are generally governed by the electronic states near the hot spots, $\xi_{\mathbf{k}_{\rm hs}} = -\xi_{\mathbf{k}_{\rm hs}+\mathbf{Q}}$, i.e., points of the Fermi surface separated by the density-wave ordering vector $\mathbf{Q}$. In this case, an appropriate momentum-dependent temperature profile can be applied to selectively melt the density-wave state while preserving other homogeneous ordered phases.

Although generic, this concept of selective melting can be nicely demonstrated by an explicit calculation for the case of competing spin-density wave (SDW) and s^{+-} superconductivity (SC) in the iron pnictides. We emphasize that our goal here is not to provide a microscopically calculated phase diagram for a specific iron pnictide material, but rather to use a transparent low-energy model to demonstrate the general concept proposed here. In this spirit, an effective low-energy model widely employed to study the SDW-SC competition in the pnictides is a two-band model with one circular hole pocket at the center of the Fe square-lattice Brillouin zone, and one elliptical electron pocket centered at the SDW ordering vector $\mathbf{Q}$ [36]. The non-interacting Hamiltonian H_0 then contains two bands that can be conveniently parametrized as $\xi_{h,\mathbf{k}} = \varepsilon_0 - \frac{k^2}{2m}$ and $\xi_{e,\mathbf{k}+\mathbf{Q}} = -\xi_{h,\mathbf{k}} - \delta_\mu - \delta_m \cos 2\theta$. The parameters δ_μ (proportional to the electronic occupation number) and δ_m (proportional to the ellipticity of the electron pocket) serve as a measure of the nesting condition between the two bands.

The two leading instabilities arising from $H_{\rm el}$ are the s^{+-} SC instability, characterized by two uniform gaps of opposite signs in the two bands, and the SDW instability. While the former is sensitive to all Fermi surface states, the latter is governed by the hot spots. When $|\delta_\mu| < |\delta_m|$, there are four pairs of hot spots located at the Fermi surface angles multiples of $\theta_{\rm hs} = \frac{1}{2}\arccos(-\delta_\mu/\delta_m)$, whereas when $|\delta_\mu| > |\delta_m|$, there are no hot spots. Thus, for a fixed δ_m, increasing δ_μ makes nesting poorer, which suppresses the SDW instability. The (δ_μ, T) equilibrium phase diagram of this model is shown by the solid lines in Fig. 3 for fixed δ_m.

The phase diagram of the non-equilibrium steady state, in which the electrons are subject to a momentum dependent temperature $\delta T\left(\theta_F\right)$, is obtained using the Keldysh formalism. As shown in the SM, the SC and SDW transition lines are obtained by effectively replacing the equilibrium distribution n_0^F in the self-consistent gap equations by the out-of-equilibrium distribution n_F (similarly to the problem of microwave enhanced superconductivity, see [10, 11, 37]). In what follows, we use the profile $\delta T\left(\theta_F\right)/\left\langle \delta T\right\rangle$ calculated in the previous section for $\kappa = 0.3$ and $\Omega_0 = 3$, corresponding to dominant heating around $\theta_F = 0, \pi/2$ (see Fig. 2b). The steady-state phase diagram is shown by the shaded regions in Fig. 3. To make the comparison with the equilibrium phase diagram more meaningful, and to highlight the impact of non-uniform heating, the equilibrium temperature was shifted by the average heating $\langle \delta T \rangle$, which depends on the external drive.

On the overdoped side of the phase diagram ($\delta_\mu/T_M \gtrsim 0.75$), where only SC is present, we find that the SC T_c is unaffected by the non-uniform heating. This is because the s^{+-} SC instability has equal contributions from all electronic states at the Fermi surface, since the gap func-

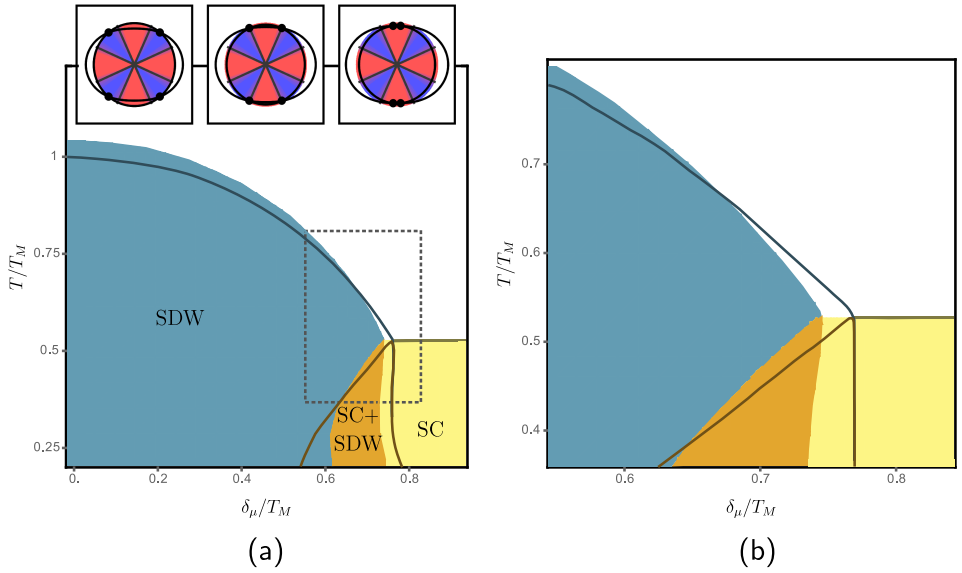

FIG. 3. **Non-equilibrium phase diagram for competing superconductivity (SC) and spin-density wave (SDW).** The steady-state non-equilibrium phase diagram for the two-band model of the iron pnictides is shown in panel (a), and the highlighted region is zoomed in panel (b). The inset shows the superimposed circular hole-like and elliptical electron-like Fermi pockets, with the latter displaced by the SDW ordering vector $\mathbf{Q}$. The crossing points are the hot spots $\mathbf{k}_{\rm hs}$, which govern the SDW instability; their positions are controlled by the parameter δ_μ, which also determines the carrier concentration. The non-equilibrium phase diagram was obtained for the anisotropic temperature profile $\delta T\,(\theta_F)$ shown in Fig. 2b ($\kappa = 0.3$) and illustrated in the inset (red and blue denote regions hotter and colder than the average heating $\langle \delta T \rangle$, respectively). For comparison, we also show the equilibrium phase diagram (solid lines) shifted by the average heating $\langle \delta T \rangle / T_M \approx 0.175$. Here, we set $\delta_m/T_M = 0.92$. All quantities are expressed in terms of the equilibrium SDW transition temperature T_M.

tion is uniform. As a result, T_c is sensitive only to the average temperature around the Fermi surface, $\langle \delta T \rangle$. In contrast, on the very underdoped side of the phase diagram (near $\delta_\mu = 0$), where only SDW is present, we observe that the SDW transition temperature T_M increases for non-uniform heating, because the SDW instability is dominated by the hot spots of the Fermi surface. For these doping levels, as shown in the inset of Fig. 3a, the hot spots are located near $\theta_F = \pi/4$, where the local temperature $\delta T(\frac{\pi}{4})$ is smaller than the average $\langle \delta T \rangle$.

As δ_μ (i.e. doping) increases, the hot spots move towards the $\theta_F = \pi/2$ direction; this behavior is also seen experimentally in certain pnictides [38]. Because the local temperature in this Fermi surface region is larger than the average one, T_M decreases. More interestingly, as highlighted in Fig. 3b, superconductivity is favored and T_c systematically increases near the optimal doping regime $\delta_\mu/T_M \approx 0.75$, as compared to the uniform heating case. Because T_c itself is unaffected by the non-uniform heating, this enhancement of T_c is a direct consequence of the suppression of the SDW transition T_M, illustrating that a momentum-dependent temperature is able to shift the balance between competing orders.

Concluding remarks – Our work demonstrates that non-equilibrium acoustic phonons excited around a well-defined energy lead to a non-uniform redistribution of electronic states around the Fermi surface, which is manifested as a momentum-dependent temperature. This robust theoretical result, which stems from geometric constraints imposed by energy and momentum conservation, together with the intrinsic anisotropy of the sound velocity, reveals a hitherto unexplored path to manipulate correlated states via pump-and-probe experiments, which have so far been mostly focusing on the coherent excitation of optical phonons. Among several possible applications of this novel concept, we showed that it can be employed to selectively melt competing electronic states, particularly in the case of unconventional superconductivity competing with a density-wave type of order. The potential enhancement of T_c by non-equilibrium acoustic phonons complements previous approaches in which SC is enhanced by optical phonons or microwave irradiation.

These results open a broad set of questions that deserve further investigation, such as the impact of non-equilibrium acoustic phonons on electronic orders that directly couple to the lattice, for instance nematic orders and charge-density waves. Furthermore, nodal superconducting states are ideal candidates to be manipulated by a momentum-dependent temperature, since the nodal quasi-particles, which determine the low-energy excitations, can experience a different local temperature than the average. Finally, while here we focused on long-range order, a non-uniform electronic temperature should also impact the low-energy charge and magnetic fluctuation spectra, which may themselves affect the pairing state.

ACKNOWLEDGMENTS

We acknowledge fruitful discussions with A. Chubukov, C. Giannetti, A. Kamenev, J. Schmalian, and I. Vishik. M.S. and R.M.F. were supported by the U.S. Department of Energy, Office of Science, Basic Energy Sciences, under Award number de-sc0012336. P.P.O. acknowledges support from Iowa State University Startup Funds. The work of A.L. was financially supported by the NSF Grants No. DMR-1606517 and ECCS-1560732. Support for this research at the University of Wisconsin-Madison was provided by the Office of the Vice Chancellor for Research and Graduate Education with funding from the Wisconsin Alumni Research Foundation.

[1] J. Orenstein, Phys. Today **65(9)**, 44 (2012).
[2] C. Giannetti, M. Capone, D. Fausti, M. Fabrizio, F. Parmigiani, and D. Mihailovic, Adv. Phys. **65**, 58 (2016).
[3] M. Rini, R. Tobey, N. Dean, J. Itatani, Y. Tomioka, Y. Tokura, R. W. Schoenlein, and A. Cavalleri, Nature **449**, 72 (2007).
[4] D. Fausti, R. I. Tobey, N. Dean, S. Kaiser, A. Dienst, M. C. Hoffmann, S. Pyon, T. Takayama, H. Takagi, and A. Cavalleri, Science **331**, 189 (2011).
[5] L. X. Yang, G. Rohde, T. Rohwer, A. Stange, K. Hanff, C. Sohrt, L. Rettig, R. Cortés, F. Chen, D. L. Feng, T. Wolf, B. Kamble, I. Eremin, T. Popmintchev, M. M. Murnane, H. C. Kapteyn, L. Kipp, J. Fink, M. Bauer, U. Bovensiepen, and K. Rossnagel, Phys. Rev. Lett. **112**, 207001 (2014).
[6] R. Mankowsky, A. Subedi, M. Forst, S. O. Mariager, M. Chollet, H. T. Lemke, J. S. Robinson, J. M. Glownia, M. P. Minitti, A. Frano, M. Fechner, N. A. Spaldin, T. Loew, B. Keimer, A. Georges, and A. Cavalleri, Nature **516**, 71 (2014).
[7] I. M. Vishik, F. Mahmood, Z. Alpichshev, J. Higgins, R. L. Greene, and N. Gedik, arXiv:1601.06694 (2016).
[8] M. Mitrano, A. Cantaluppi, D. Nicoletti, S. Kaiser, A. Perucchi, S. Lupi, P. Di Pietro, D. Pontiroli, M. Riccò, S. R. Clark, D. Jaksch, and A. Cavalleri, Nature **530**, 461 (2016).
[9] E. E. M. Chia, D. Talbayev, J.-X. Zhu, H. Q. Yuan, T. Park, J. D. Thompson, C. Panagopoulos, G. F. Chen, J. L. Luo, N. L. Wang, and A. J. Taylor, Phys. Rev. Lett. **104**, 027003 (2010).
[10] G. M. Eliashberg, Sov. Phys. JETP **11**, 696 (1960).
[11] G. M. Eliashberg and B. I. Ivlev, in *Nonequilibrium superconductivity*, Modern problems in condensed matter sciences, Vol. 12, edited by D. Langenberg and A. Larkin (North-Holland, 1986) Chap. 6, pp. 211–251.
[12] J. A. Pals, K. Weiss, P. M. T. M. van Attekum, R. E. Horstman, and J. Wolter, Phys. Rep. **89**, 323 (1982).
[13] A. Subedi, A. Cavalleri, and A. Georges, Phys. Rev. B **89**, 220301 (2014).
[14] W. Fu, L.-Y. Hung, and S. Sachdev, Phys. Rev. B **90**, 024506 (2014).
[15] A. Moor, P. A. Volkov, A. F. Volkov, and K. B. Efetov, Phys. Rev. B **90**, 024511 (2014).
[16] M. Dzero, M. Khodas, and A. Levchenko, Phys. Rev. B **91**, 214505 (2015).
[17] Z. M. Raines, V. Stanev, and V. M. Galitski, Phys. Rev. B **91**, 184506 (2015).
[18] G. Goldstein, C. Aron, and C. Chamon, Phys. Rev. B **91**, 054517 (2015).
[19] Y. Wang, B. Moritz, C.-C. Chen, C. J. Jia, M. van Veenendaal, and T. P. Devereaux, Phys. Rev. Lett. **116**, 086401 (2016).
[20] M. Knap, M. Babadi, G. Refael, I. Martin, and E. Demler, Phys. Rev. B **94**, 214504 (2016).
[21] M. A. Sentef, A. Tokuno, A. Georges, and C. Kollath, arXiv:1611.04307 (2016).
[22] D. M. Kennes, E. Y. Wilner, D. R. Reichman, and A. J. Millis, arXiv:1609.03802 (2016).
[23] A. F. Kemper, M. A. Sentef, B. Moritz, T. P. Devereaux, and J. K. Freericks, arXiv:1609.00087 (2016).
[24] M. Babadi, M. Knap, I. Martin, G. Refael, and E. Demler, arXiv:1702.02531 (2017).
[25] T. Pezeril, G. Saini, D. Veysset, S. Kooi, P. Fidkowski, R. Radovitzky, and K. A. Nelson, Phys. Rev. Lett. **106**, 214503 (2011).
[26] A. D. Caviglia, R. Scherwitzl, P. Popovich, W. Hu, H. Bromberger, R. Singla, M. Mitrano, M. C. Hoffmann, S. Kaiser, P. Zubko, S. Gariglio, J.-M. Triscone, M. Först, and A. Cavalleri, Phys. Rev. Lett. **108**, 136801 (2012).
[27] M. Forst, A. D. Caviglia, R. Scherwitzl, R. Mankowsky, P. Zubko, V. Khanna, H. Bromberger, S. B. Wilkins, Y.-D. Chuang, W. S. Lee, W. F. Schlotter, J. J. Turner, G. L. Dakovski, M. P. Minitti, J. Robinson, S. R. Clark, D. Jaksch, J.-M. Triscone, J. P. Hill, S. S. Dhesi, and A. Cavalleri, Nat Mater **14**, 883 (2015).
[28] R. M. Fernandes, A. V. Chubukov, and J. Schmalian, Nature Physics **10**, 97 (2014).
[29] E. Fradkin, S. A. Kivelson, M. J. Lawler, J. P. Eisenstein, and A. P. Mackenzie, Annual Review of Condensed Matter Physics **1**, 153 (2010).
[30] R. M. Fernandes, D. K. Pratt, W. Tian, J. Zarestky, A. Kreyssig, S. Nandi, M. G. Kim, A. Thaler, N. Ni, P. C. Canfield, R. J. McQueeney, J. Schmalian, and A. I. Goldman, Phys. Rev. B **81**, 140501 (2010).
[31] J. Chang, E. Blackburn, A. T. Holmes, N. B. Christensen, J. Larsen, J. Mesot, R. Liang, D. A. Bonn, W. N. Hardy, A. Watenphul, M. v. Zimmermann, E. M. Forgan, and S. M. Hayden, Nat Phys **8**, 871 (2012).
[32] L. D. Pham, T. Park, S. Maquilon, J. D. Thompson, and Z. Fisk, Phys. Rev. Lett. **97**, 056404 (2006).
[33] U. Karahasanovic and J. Schmalian, Phys. Rev. B **93**, 064520 (2016).
[34] J. Wang, Y. Hashimoto, J. Kono, A. Oiwa, H. Munekata, G. D. Sanders, and C. J. Stanton, Phys. Rev. B **72**, 153311 (2005).
[35] V. V. Kabanov and A. S. Alexandrov, Phys. Rev. B **78**, 174514 (2008).
[36] R. M. Fernandes and A. V. Chubukov, Rep. Prog. Phys. **80**, 014503 (2017).
[37] A. Robertson and V. M. Galitski, Phys. Rev. A **80**, 063609 (2009).

[38] C. Liu, T. Kondo, R. M. Fernandes, A. D. Palczewski, E. D. Mun, N. Ni, A. N. Thaler, A. Bostwick, E. Rotenberg, J. Schmalian, S. L. Bud'ko, P. C. Canfield, and A. Kaminski, Nat Phys **6**, 419 (2010).
[39] R. M. Fernandes and J. Schmalian, Phys. Rev. B **82**, 014521 (2010).
[40] A. B. Vorontsov, M. G. Vavilov, and A. V. Chubukov, Phys. Rev. B **81**, 174538 (2010).
[41] A. Levchenko and A. Kamenev, Phys. Rev. B **76**, 094518 (2007).
[42] A. Kamenev, *Field Theory of Non-Equilibrium Systems* (Cambridge University Press, 2011).

Appendix A: Derivation of the anisotropic sound velocity and electron-phonon matrix element

Our starting point is the elastic free energy of a tetragonal system written in terms of the Fourier components of the strain fields, $u_{ij} = (q_i u_j + q_j u_i)/2$

$$F = \sum_{ij} u_i \mathcal{M}_{ij}(\mathbf{q}) u_j \tag{A1}$$

where $\mathcal{M}_{ij}(\mathbf{q})$, the symmetric dynamic matrix describing the long wavelength phonon modes, is given by [33]:

$$\mathcal{M}_{ij}(\mathbf{q}) = \begin{pmatrix} C_{11}q_x^2 + C_{66}q_y^2 + C_{44}q_z^2 & (C_{11}+C_{66})q_xq_y & (C_{13}+C_{14})q_xq_z \\ (C_{12}+C_{66})q_xq_y & C_{66}q_x^2 + C_{11}q_y^2 + C_{44}q_z^2 & (C_{13}+C_{44})q_yq_z \\ (C_{13}+C_{44})q_yq_z & (C_{13}+C_{14})q_xq_z & C_{44}(q_x^2+q_y^2) + C_{33}q_z^2 \end{pmatrix} \tag{A2}$$

Hereafter we focus on the square lattice, setting $q_z = 0$. Introducing the notation $\mu_1 = C_{11} + C_{66}$, $\mu_2 = C_{11} - C_{66}$, and $\mu_3 = C_{12} + C_{66}$, diagonalization of the dynamic matrix leads to the two in-plane acoustic phonon modes:

$$\omega_\pm^2(\mathbf{q}) = \frac{1}{\sqrt{2\rho}}\mathbf{q}^2 \left(\mu_1 \pm \sqrt{\mu_2^2\cos^2(2\varphi) + \mu_3^2\sin^2(2\varphi)}\right) \tag{A3}$$

where ρ is the density. For convenience we introduce $x^2 = \mu_2^2\cos^2(2\varphi) + \mu_3^2\sin^2(2\varphi) = \frac{1}{2}(\mu_2^2+\mu_3^2) + \frac{1}{2}(\mu_2^2-\mu_3^2)\cos(4\varphi)$, which allows us to express the sound velocity according to: $v_{s,\lambda} = \sqrt{\mu_1 + \lambda x}$. As for the eigenvectors, which give the polarization of the phonon modes, they are given by:

$$\mathbf{e}_+(\varphi) = \frac{1}{\sqrt{2x\,(x+\mu_2\cos 2\varphi)}}\begin{pmatrix}\mu_2\cos 2\varphi + x \\ \mu_3 \sin 2\varphi\end{pmatrix}; \qquad \mathbf{e}_-(\varphi) = \frac{1}{\sqrt{2x\,(x+\mu_2\cos 2\varphi)}}\begin{pmatrix}-\mu_3\sin 2\varphi \\ \mu_2\cos 2\varphi + x\end{pmatrix} \tag{A4}$$

Note that the polarization becomes particularly simple along the high-symmetry directions (assuming $\mu_2 > 0$, as it is the case for instance in iron pnictides): $\mathbf{e}_\pm(\pi/4) = (\pm 1, 1)/\sqrt{2}$, $\mathbf{e}_+(0) = (1,0)$ and $\mathbf{e}_-(0) = (0,1)$. Thus, while the polarization $\mathbf{e}_+$ is mostly longitudinal, $\mathbf{e}_-$ is mostly transversal.

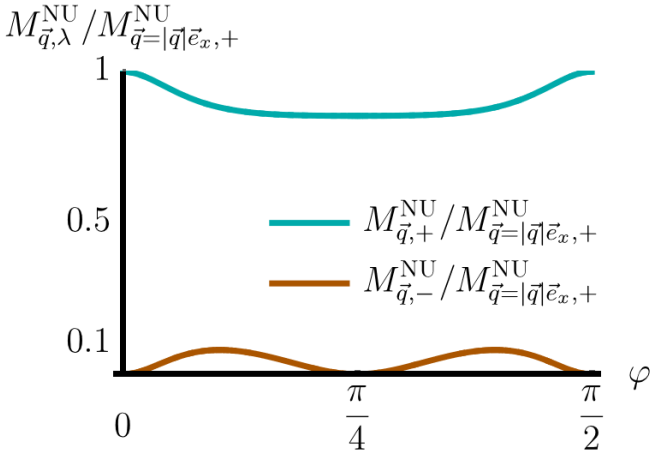

FIG. 4. The absolute value of the no-umklapp matrix element, $\left(M^{\rm NU}_{\mathbf{q}+\mathbf{G},-}\right)^2$, normalized to the matrix element of the $\lambda = +$ branch in the $\mathbf{q} = q\mathbf{e}_x$ direction, as function of the phonon propagation direction φ. In this and in the next figures, we set the ratio $\frac{(C_{11}-C_{12})/2}{C_{66}} = \frac{1}{4}$.

As for the electron-phonon matrix element, while a full quantitative description depends on microscopic details, in the case of acoustic phonons it is usually approximated by:

$$M_{\mathbf{k}-\mathbf{k}',\mathbf{q},\lambda} = \sqrt{\frac{\hbar}{2V\rho\omega_{q,\lambda}}}\sum_{\mathbf{G}}\delta(\mathbf{k}-\mathbf{k}'-\mathbf{q}-\mathbf{G})\times \\ \times\left[\mathbf{e}_{\mathbf{q},\lambda}\cdot(\mathbf{q}+\mathbf{G})\right]K(|\mathbf{q}+\mathbf{G}|) \tag{A5}$$

Here, $K(q)$ is a function that satisfies $K(|\mathbf{G}+\mathbf{q}|) \propto q$ for $q \ll G$ and any reciprocal lattice vector $\mathbf{G}$. In the case $\mathbf{G} = 0$, $K(q \to 0)$ remains constant. Now, because the low-energy phonon mode $\lambda = -$ is mostly transversal, the matrix element nearly vanishes in the absence of umklapp, since

$$\left(M^{\rm NU}_{\mathbf{q},-}\right)^2 = \frac{\hbar K_0^2 q^2}{2V\rho\omega_{q,-}}\left(\mathbf{e}_{\mathbf{q},-}\cdot\hat{\mathbf{q}}\right)^2 \propto \frac{q\left(\mathbf{e}_{\mathbf{q},-}\cdot\hat{\mathbf{q}}\right)^2}{v_{s,-}(\varphi)} \tag{A6}$$

where the superscript NU means no-umklapp. This is illustrated in Fig. 4, where we plot $\left(M^{\rm NU}_{\mathbf{q},-}\right)^2$. Note that, the closest the system is to a tetragonal-to-orthorhombic phase transition, in which $C_{11} - C_{12} \to 0$, the smallest $\left(M^{\rm NU}_{\mathbf{q},\lambda}\right)^2$ is. It is important to emphasize that the electron-phonon matrix element given in Eq. (A5) is an approximation. For non-spherical Fermi surfaces, for in-

stance, coupling to transversal modes is more natural, but still suppressed.

Given the smallness of $\left(M^{\mathrm{NU}}_{\mathbf{q},\lambda}\right)^2$, it is natural to consider the umklapp contribution, particularly since it remains non-zero even when $C_{11}-C_{12}\to 0$. Because the function $K(|\mathbf{q}+\mathbf{G}|)$ usually decays quickly for larger G, we here consider just the reciprocal vectors with smallest amplitudes, namely $\mathbf{G}=(\pm 2\pi,0),(0,\pm 2\pi)$. In this case, in the long wavelength limit ($q\to 0$), we find:

$$\left(M^{\mathrm{U}}_{\mathbf{q}+\mathbf{G},-}\right)^2=\frac{\hbar K_G^2 q^2}{2V\rho\omega_{q,-}}\sum_i\left(\mathbf{e}_{\mathbf{q},-}\cdot\mathbf{G}_i\right)^2\propto\frac{q}{v_{s,-}(\varphi)} \tag{A7}$$

where, in the last step, we used the fact that for the set of reciprocal lattice vectors considered here, $\left(\mathbf{e}_{\mathbf{q},-}\cdot\mathbf{G}_i\right)^2=2G\left(e_x^2+e_y^2\right)=2G$. Therefore, in this approximation, the anisotropy of the matrix element arises solely from the sound velocity.

Generically, we can then write the matrix element as a combination of umklapp and no-umklapp contributions:

$$M_{\mathbf{k}-\mathbf{k}',\mathbf{q},\lambda}=M^{\mathrm{NU}}_{\mathbf{q},\lambda}\delta(\mathbf{k}-\mathbf{k}'-\mathbf{q})+M^{\mathrm{U}}_{\mathbf{q}+\mathbf{G},\lambda}\delta(\mathbf{k}-\mathbf{k}'-\mathbf{q}-\mathbf{G}). \tag{A8}$$

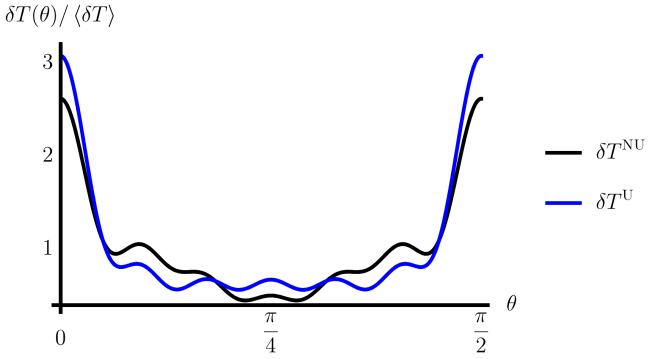

FIG. 5. Comparison of the normalized temperature profiles $\delta T(\theta)/\langle\delta T\rangle$ arising from the umklapp (U) and no-umklapp (NU) processes for the parameters $\Omega_0=3$ and $\kappa=0.3$.

In our calculations, we considered only the $M^{\mathrm{U}}_{\mathbf{q}+\mathbf{G},\lambda}$ contribution, since it is the only one that remains non-zero even in the case of a strongly anisotropic sound velocity (i.e. when $(C_{11}-C_{12})/2\ll C_{66}$). We however also computed the anisotropic temperature profile $\delta T(\theta_F)$ that arises from the no-unklapp contribution $M^{\mathrm{NU}}_{\mathbf{q},\lambda}$ only. As shown in Fig. 5, the resulting normalized temperature profile is almost identical to that obtained from the umklapp contribution for the case $\kappa=0.3$ and $\Omega_0=3$ (which was used to calculate the steady-state phase diagram of the main text). This indicates that the main source of anisotropy in the matrix element indeed arises from the denominator, i.e. from the sound velocity.

Appendix B: Solution of the Boltzmann equation

As discussed in the main text, the Boltzmann equation is given by:

$$I^{\mathrm{phonon}}_{\mathrm{coll}}[n^F,n^B]=-\sum_{\alpha=\pm}\alpha\int\frac{\mathrm{d}^2p'}{(2\pi)^2}\delta(\xi_{\mathbf{p}}-\xi_{\mathbf{p}'}-\alpha\omega_{\mathbf{p}-\mathbf{p}'})|M_{\mathbf{p}-\mathbf{p}'}|^2\left[n^F_{\xi_{\mathbf{p}}}n^F_{-\xi_{\mathbf{p}'}}n^B_{-\alpha\omega_{\mathbf{p}-\mathbf{p}'}}+n^F_{-\xi_{\mathbf{p}}}n^F_{\xi_{\mathbf{p}'}}n^B_{\alpha\omega_{\mathbf{p}-\mathbf{p}'}}\right]=0 \tag{B1}$$

Linearization of the kernel leads to

$$\left[n^F_{\xi_{\mathbf{p}}}n^F_{-\xi_{\mathbf{p}'}}n^B_{-\alpha\omega_{\mathbf{p}-\mathbf{p}'}}+n^F_{-\xi_{\mathbf{p}}}n^F_{\xi_{\mathbf{p}'}}n^B_{\alpha\omega_{\mathbf{p}-\mathbf{p}'}}\right]\approx-\frac{1}{8}\frac{h^F_{\xi_{\mathbf{p}}}-h^F_{\xi_{\mathbf{p}'}}-\alpha h^B_{\omega_{\mathbf{p}-\mathbf{p}'}}}{\cosh\left[\frac{\beta\xi_{\mathbf{p}}}{2}\right]\cosh\left[\frac{\beta\xi_{\mathbf{p}'}}{2}\right]\sinh\left[\frac{\beta\alpha\omega_{\mathbf{p}-\mathbf{p}'}}{2}\right]} \tag{B2}$$

where we used the fact that $h^B_{\alpha\omega_q}=\alpha h^B_{\omega_q}$. Our goal is to find the fermionic distribution h^F that solves the Boltzmann equation for a given phononic distribution h^B. It is convenient to work with a functional $\mathcal{F}\left[h^F\right]$ whose minimization with respect to h^F gives the Boltzmann equation. We find:

$$\mathcal{F}\left[h^F\right]=\int\frac{\mathrm{d}^2p}{(2\pi)^2}\int\frac{\mathrm{d}^2p'}{(2\pi)^2}\sum_{\alpha=\pm}\alpha\delta(\xi_{\mathbf{p}}-\xi_{\mathbf{p}'}-\alpha\omega_{\mathbf{p}-\mathbf{p}'})\frac{|M_{\mathbf{p}-\mathbf{p}'}|^2}{16}\frac{\left(h^F_{\xi_{\mathbf{p}}}-h^F_{\xi_{\mathbf{p}'}}\right)^2-2\alpha h^B_{\mathbf{p}-\mathbf{p}'}h^F_{\xi_{\mathbf{p}}}+2\alpha h^B_{\mathbf{p}'-\mathbf{p}}h^F_{\xi_{\mathbf{p}'}}}{\cosh\left[\frac{\xi_{\mathbf{p}}}{2T}\right]\cosh\left[\frac{\xi_{\mathbf{p}'}}{2T}\right]\sinh\left[\frac{\xi_{\mathbf{p}}-\xi_{\mathbf{p}'}}{2T}\right]} \tag{B3}$$

To proceed, we note that, since the energy of the excited acoustic phonons is much smaller than the Fermi energy, we can linearize the electronic dispersion in the vicinity of the Fermi surface. Then, it is convenient to split the momentum into components perpendicular and parallel to the Fermi surface (FS), yielding $\int\mathrm{d}^2p/(2\pi)^2=\int\mathrm{d}\theta/(2\pi)N_F(\theta)\int\mathrm{d}\xi_p$. As a result, the electronic states close to the Fermi level, the phonon dispersion, and the electron-phonon-matrix

element Eq. (A5) depend only on the transferred momenta longitudinal to the Fermi surface θ and θ'. For simplicity, hereafter we will keep the notation $\omega_q = \omega_{\mathbf{p}_F(\theta)-\mathbf{p}_F(\theta')}$. Finally, introducing the parametetrization $h^F_{\mathbf{p}} = \delta\mu_{\hat{\mathbf{p}}} + \frac{\xi_{\mathbf{p}}}{T}\,\delta T_{\hat{\mathbf{p}}}$, we can evaluate the energy integration in the functional Eq. (B3), obtaining a functional that depends only on the longitudinal momenta:

$$\mathcal{F}\left[h^F\right] = \iint \frac{\mathrm{d}\theta\mathrm{d}\theta'}{(2\pi)^2} N_F(\theta)N_F(\theta')\frac{\omega_q|M_{\mathbf{q}}|^2}{4\sinh^2(\frac{\beta\omega_q}{2})}\left\{\left(\frac{\beta\omega_q}{2}\right)^2\left[(\delta T_{\hat{\mathbf{p}}}+\delta T_{\hat{\mathbf{p}}'})\right]^2 + \frac{1}{3}\left[\pi^2+\left(\frac{\beta\omega_q}{2}\right)^2\right](\delta T_{\hat{\mathbf{p}}}-\delta T_{\hat{\mathbf{p}}'})^2 - \beta\omega_q h^B_{\mathbf{q}}\left[\delta T_{\hat{\mathbf{p}}}+\delta T_{\hat{\mathbf{p}}'}\right]\right\} \quad \text{(B4)}$$

Because the chemical potential $\delta\mu_{\hat{\mathbf{p}}}$ does not appear in the functional, it follows that a non-equilibrium distribution of acoustic phonons cannot change the chemical potential. Note that while small momentum scattering is suppressed by the electron-phonon matrix element Eq (A7), this effect is compensated by the amount of available thermal states to scatter, which is proportional to $1/\sinh^2(\beta\omega_q/2)$.

To minimize the functional, it is convenient to use the Fourier representation of $\delta T\,(\theta)$:

$$\delta T(\theta) - \delta T(\theta') = -2\sum_n \delta T_n \sin\left(n\frac{\theta-\theta'}{2}\right)\sin\left(n\frac{\theta+\theta'}{2}\right) \quad \text{(B5a)}$$

$$\delta T(\theta) + \delta T(\theta') = 2\sum_n \delta T_n \cos\left(n\frac{\theta-\theta'}{2}\right)\cos\left(n\frac{\theta+\theta'}{2}\right) \quad \text{(B5b)}$$

The Fourier components δT_n can then be found by solving the matrix equation $\sum_m K_{nm}\delta T_m = D_n$, with:

$$D_n = -\iint \frac{\mathrm{d}\theta\mathrm{d}\theta'}{(2\pi)^2} N_F(\theta)N_F(\theta')\frac{\omega_q|M_{\mathbf{q}}|^2}{4\sinh^2(\frac{\beta\omega_q}{2})} 2\beta\omega_q h^B(\omega_q)\cos\left(n\frac{\theta-\theta'}{2}\right)\cos\left(n\frac{\theta+\theta'}{2}\right) \quad \text{(B6)}$$

and

$$K_{nm} = \iint \frac{\mathrm{d}\theta\mathrm{d}\theta'}{(2\pi)^2} N_F(\theta)N_F(\theta')\frac{\omega_q|M_{\mathbf{q}}|^2}{4\sinh^2(\frac{\beta\omega_q}{2})} \left\{\left(\frac{\beta\omega_q}{2}\right)^2 4\cos\left(n\frac{\theta-\theta'}{2}\right)\cos\left(n\frac{\theta+\theta'}{2}\right)\cos\left(m\frac{\theta-\theta'}{2}\right)\cos\left(m\frac{\theta+\theta'}{2}\right) + \frac{1}{3}\left[\pi^2+\left(\frac{\beta\omega_q}{2}\right)^2\right] 4\sin\left(n\frac{\theta-\theta'}{2}\right)\sin\left(n\frac{\theta+\theta'}{2}\right)\sin\left(m\frac{\theta-\theta'}{2}\right)\sin\left(m\frac{\theta+\theta'}{2}\right)\right\} \quad \text{(B7)}$$

In the main text, we numerically solved these equations using the following expressions for the phononic distribution function and matrix element:

$$h^B(\omega_q) = W_B\,\frac{\delta}{\delta^2 + \left[\frac{\omega_q}{2T}-\Omega_0\right]^2} \quad \text{(B8)}$$

$$\omega_q|M_{\mathbf{q}}|^2 = m_0 q^2 = \tilde{m}_0 \sin\left(\frac{\theta-\theta'}{2}\right) \quad \text{(B9)}$$

Note that the overall factor m_0 drops from the equations, since it appears as a constant in both K_{nm} and D_n. The phonon energy is given in terms of the dimensionless parameters and the function $\tilde{v}_s$ defined in the main text:

$$\frac{1}{2}\beta\omega_q = \frac{\Omega_0}{\kappa}\,\tilde{v}_s\left(\frac{\theta+\theta'}{2}\right)\sin\left(\frac{\theta-\theta'}{2}\right) \quad \text{(B10)}$$

Consequently, the functional depends only on three parameters, Ω_0, δ, and κ. Prefactors appearing in h^B, in the matrix element $|M_{\mathbf{q}}|^2$, and in the density of states can be conveniently absorbed into the average heating $\langle\delta T\rangle$.

Appendix C: Analysis of the geometric constraint

In the main text, we derived the geometric constraint on the initial and final electronic momenta θ_F, θ'_F due to the energy-momentum conservation associated with electron-phonon scattering:

$$\kappa = \tilde{v}_s\left(\frac{\theta_F+\theta'_F}{2}\right)\sin\left(\frac{\theta_F-\theta'_F}{2}\right) \quad \text{(C1)}$$

An important quantity is the density of available scattering states θ'_F for a given momentum θ_F, which we denoted by $N(\theta_F)$. For a given angle θ_0 in the first quadrant, there are at least two angles θ_1 and θ_2 also in the first quadrant that satisfy Eq. (C1), with $\theta_1 > \theta_0 > \theta_2$. In order to determine $N(\theta_F)$, let us introduce two "rotated" variables $\delta\theta = (\theta_1 - \theta_2)/2$ and $\varphi = (\theta_1 + \theta_2)/2$, such that condition (C1) becomes $\kappa = \tilde{v}_s(\varphi)\sin(\delta\theta)$. Note that φ is, up to a translation by $\pi/2$, the angle corresponding to the phonon propagation direction. In terms of these variables, it is straightforward to obtain the solution to Eq. (C1), $\delta\theta(\varphi) = \arcsin(\kappa/\tilde{v}_s(\varphi))$. Thus, for a given phonon direction φ, the two electronic scattering angles are given by $\theta_{1/2} = \Phi_\pm(\varphi)$, with $\Phi_\pm(\varphi) = \varphi \pm \delta\theta(\varphi)$.

It is now straightforward to count the number of all possible electronic scattering pairs by integrating over all available phonon directions:

$$N(\theta) = \frac{1}{2}\sum_{\alpha=\pm1}\int \mathrm{d}\varphi\, \delta\left[\theta - \Phi_\alpha(\varphi)\right]. \tag{C2}$$

yielding:

$$N(\theta) = \frac{1}{2}\sum_{\alpha=\pm1}\frac{1}{1+\alpha\left(\frac{\partial\delta\theta}{\partial\varphi}\right)_{\varphi=\Phi_\alpha^{-1}(\theta)}} \tag{C3}$$

Alternatively, we can also express the density of scattering states as function of the phonon direction φ. In this case,

$$\begin{aligned} N(\varphi) &= \frac{1}{2}\left[\left(\frac{\partial\phi(\varphi)}{\partial\varphi_q}\right)^{-1} + \left(\frac{\partial\phi'(\varphi)}{\partial\varphi_q}\right)^{-1}\right] \\ &= \frac{1}{1-\frac{\kappa^2}{\tilde{v}_s^2-\kappa^2}\left(\frac{\tilde{v}'_s}{\tilde{v}_s}\right)^2}. \end{aligned} \tag{C4}$$

In Fig. 2 of the main text, we plotted $N(\theta)$ for different values of κ. Note that for $\kappa > \min_{\varphi\in[0,\pi/2]}\sqrt{\frac{v_s^4}{v_s^2+(v'_s)^2}}$ the expressions above do not apply and the density needs to be redefined, since for a given angle φ, four different pairs (θ_F, θ'_F) exist. In our case this happens for about $\kappa \approx 0.365$.

In Fig. 6, we plot the density of available scattering solutions as function of the phonon direction φ, $N(\varphi)$. Clearly, for all values of κ, the main contribution comes from phonons with $\varphi \approx \varphi_0$, where φ_0 is the angle for which $\sqrt{\frac{v_s^4}{v_s^2+(v'_s)^2}}$ is minimal. In our case $\varphi_0 \approx 0.19\pi$. This observation also explains why the corrections to the matrix element arising from non-umklapp processes are not significant, as the phonon directions responsible for the anisotropic heating do not correspond to the high symmetry directions $\varphi = 0$, $\pi/4$ or $\pi/2$.

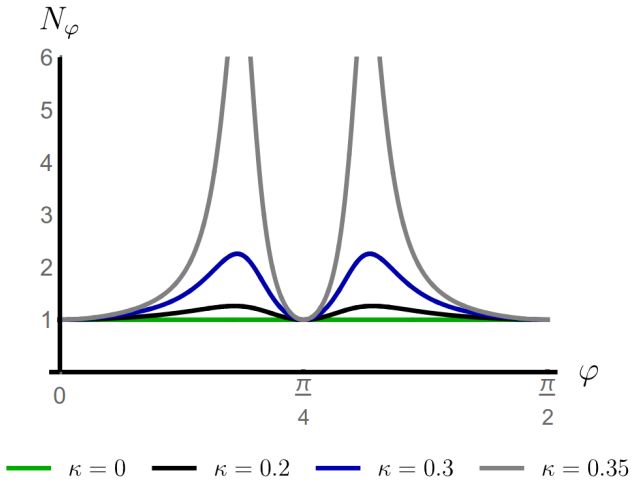

FIG. 6. The scattering density as a function of the phonon direction φ, as given by Eq. (C4).

Appendix D: Steady-state phase diagram

The interacting Hamiltonian H_{int} of the two-band model contains five different types of inter-pocket and intra-pocket interactions. To study the competition between SC and SDW, these interactions are projected in the leading electronic instabilities [36]. The complete phase diagram for the two-band model discussed in the main text can be obtained by solving the coupled non-linear self-consistent gap equations for the s^{+-} SC gap, $\Delta = -V_{\mathrm{SC}}\sum_{\mathbf{k}}\langle c_{h,-\mathbf{k}\downarrow}c_{h,\mathbf{k}\uparrow}\rangle = V_{\mathrm{SC}}\sum_{\mathbf{k}}\langle c_{e,-\mathbf{k}\downarrow}c_{e,\mathbf{k}\uparrow}\rangle$, and the SDW order parameter $M = -V_{\mathrm{SDW}}\sum_{\mathbf{k},\sigma}\left\langle c^\dagger_{h,\mathbf{k}\sigma}\sigma c_{e,\mathbf{k}\sigma}\right\rangle$. Here, for convenience, all momenta are measured with respect to the center of the respective Fermi pocket: $\mathbf{K} = 0$ for the hole pocket and $\mathbf{K} = \mathbf{Q}$ for the electron pocket. The equilibrium phase diagram of this model was previously calculated in Refs. [39, 40]. Here, because we are interested in the normal-state instabilities of the system, we do not consider the full non-linear gap equations, but instead expand to cubic order in the order parameters. The reason why we need to go to cubic order instead of simply linear order is to capture the effects of the competition between SDW and SC. The coefficients of the gap equations can be obtained directly from the Ginzburg-Landau energy functional:

$$F = \frac{a_M}{2}M^2 + \frac{u_M}{4}M^4 + \frac{a_\Delta}{2}\Delta^2 + \frac{u_\Delta}{4}\Delta^4 + \frac{\gamma}{2}M^2\Delta^2\,. \tag{D1}$$

Previously, these coefficients were computed for the two-band microscopic model in the equilibrium case [39, 40]. Our goal here is to show that, in the non-equilibrium steady-state case, the coefficients have the same functional form, but with the Fermi-Dirac equilibrium distribution function replaced by the non-equilibrium distribution function that results from the Boltzmann equation

– a procedure widely employed in the literature [10, 11].

To accomplish this, we use the Keldysh formalism [41, 42]. In this case, besides the standard advanced and retarded Green's functions, G^A and G^R, respectively, one needs to include also the Keldysh Green's function G^K. In situations close to equilibrium, as it is our case, the latter is related to the former by $G^K = f(G^R - G^A)$, where f is the symmetrized non-equilibrium distribution function, $f(\xi) = 1 - 2n_F(\xi)$. Within the Keldysh formalism, the quadratic and quartic terms of the semi-classical energy functional Eq. (D1) must be rewritten in terms of classical and quantum source components as $M^{cl}M^q$ ($\Delta^{cl}\Delta^q$) and $M^{cl}M^{cl}M^{cl}M^q$ ($\Delta^{cl}\Delta^{cl}\Delta^{cl}\Delta^q$) in order for the classical saddle point equations to be obtained via the constraints on the action $\delta S/\delta M^q|_{M^q=0} = 0$ and $\delta S/\delta\Delta^q|_{\Delta^q=0} = 0$. For the classical saddle point the RKA-rule applies, which implies the following causal combination of the Green's functions in the quartic coefficients: $RRRK + RRKA + RKAA + KAAA$.

Using τ-matrices for the band space and σ for the particle-hole space, the relevant Green's functions are expressed as:

$$\mathbb{G}^{R(K,A)}_{j,\alpha} = \sum_{j,\alpha} \mathbb{P}_{j,\alpha} G^{R(K,A)}_{j,\alpha} \tag{D2}$$

where $G^{R(A)}_{j,\alpha} = \mathrm{Lim}_{\delta\to 0^+}(\epsilon - \alpha\xi_j \pm i\delta)^{-1}$, $\mathbb{P}_{j,\alpha} = (1 + j\tau_z)(1 + \alpha\sigma_z)/4$ and $j, \alpha \in \{+, -\}$. For convenience of notation, hereafter the hole-like band is associated with $j = -1$ and the electron-like band is associated with $j = +1$. The resulting Ginzburg-Landau coefficients are then given by:

$$a_m = V_{\mathrm{SDW}} - 2i\mathrm{Tr}\left[\mathbb{G}^{\mu}_{-j,\alpha}\tau_x\mathbb{G}^{\nu}_{j,\alpha}\tau_x\right] \tag{D3a}$$

$$a_\Delta = V_{\mathrm{SC}} - 2i\mathrm{Tr}\left[\mathbb{G}^{\mu}_{j,\alpha}\sigma_x\mathbb{G}^{\nu}_{j,-\alpha}\sigma_x\right] \tag{D3b}$$

$$u_m = -2i\mathrm{Tr}\left[\mathbb{G}^{\mu}_{-j,\alpha}\tau_x\mathbb{G}^{\nu}_{j,\alpha}\tau_x\mathbb{G}^{\beta}_{-j,\alpha}\tau_x\mathbb{G}^{\lambda}_{j,\alpha}\tau_x\right] \tag{D3c}$$

$$u_{\Delta_i} = -2i\mathrm{Tr}\left[\mathbb{G}^{\mu}_{j,\alpha}\sigma_x\mathbb{G}^{\nu}_{j,-\alpha}\sigma_x\mathbb{G}^{\beta}_{j,\alpha}\sigma_x\mathbb{G}^{\lambda}_{j,\alpha}\sigma_x\right] \tag{D3d}$$

$$\gamma = 2i\Big\{\mathrm{Tr}\left[\mathbb{G}^{\mu}_{j,\alpha}\sigma_x\mathbb{G}^{\nu}_{j,-\alpha}\sigma_x\mathbb{G}^{\beta}_{j,\alpha}\tau_x\mathbb{G}^{\lambda}_{-j,\alpha}\tau_x\right] - \mathrm{Tr}\left[\mathbb{G}^{\mu}_{j,\alpha}\sigma_x\mathbb{G}^{\nu}_{j,-\alpha}\tau_x\mathbb{G}^{\beta}_{-j,-\alpha}\sigma_x\mathbb{G}^{\lambda}_{-j,\alpha}\tau_x\right]\Big\} \tag{D3e}$$

In all these expressions, the trace $\mathrm{Tr}[\ldots]$ implies summation over all indices, namely $\mathrm{Tr}[\ldots] = \sum_{j,\alpha}\int\frac{\mathrm{d}\omega}{2\pi}\int(\mathrm{d}p)\,\mathrm{tr}[\ldots]$, as well as the Keldysh indices (Greek letters). The summation over the latter satisfies the RKA rule, which means that for (μ,ν), only (R,K) and (K,A) are involved.

In order to evaluate the quartic coefficients, it is useful to consider the generic combination of four Green's functions:

$$\Gamma = 2i\int\frac{\mathrm{d}\omega}{2\pi}\int(\mathrm{d}p)\,\mathrm{tr}\left[\mathbb{P}_a\mathbb{P}_b\mathbb{P}_c\mathbb{P}_d\right]\sum_{\substack{\mu\nu\beta\lambda\\ \mathrm{RKA-Rule}}} G^{\mu}_a G^{\nu}_b G^{\beta}_c G^{\lambda}_d \tag{D4}$$

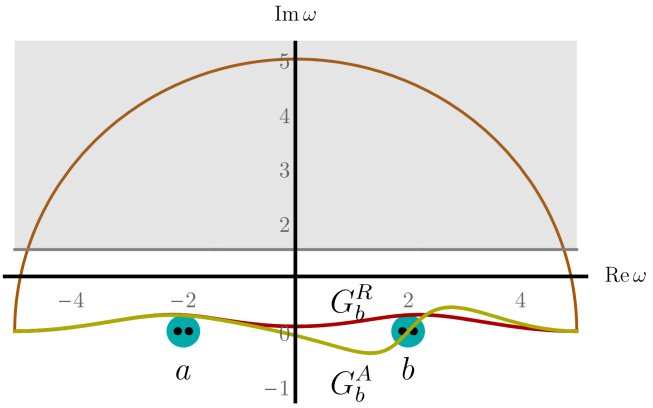

FIG. 7. Illustration of the contour integration that allows to extract the relations used to determine the out of equilibrium coefficients in Eq. (D5a). The gray area contains the features of the unknown function f and the turquoise area corresponds to the degenerate pole, which might only be resolved by causality. As a consequence, the difference between retarded and advanced components (as typically appearing from the Keldysh Green's function) is given by the residue of single poles or multiple poles.

Here, the Latin letters correspond to the combined band and particle-hole indices, whereas the Greek letters refer to Keldysh indices. Note that due to the RKA-rule, only one of the Green's functions is a Keldysh Green's function, as explained above. As a result, only the residue of the Keldysh Green's function matters, since the Keldysh component is strongly peaked at the Fermi level, $\mathrm{Lim}_{\delta\to 0} G^R_a - G^A_a = -2\pi i\delta(\epsilon - \xi_a)$. If, as in our case, two of the Greens functions share the same band/particle-hole index a, a simple evaluation by means of a Dirac delta function is no longer possible. Instead, one can use the identities:

$$\mathrm{Lim}_{\delta\to 0}\, 2i\int\frac{\mathrm{d}\omega}{2\pi}G^R_a G^R_b G^R_a G^K_b = 2\,\mathrm{Re}\,\mathrm{Lim}_{\delta\to 0}\,\mathrm{Res}_{G^A_b,\mathrm{pole}}\left(G^R_a G^R_b G^R_a G^A_b f_b(\omega)\right), \tag{D5a}$$

$$\mathrm{Lim}_{\delta\to 0}\, 2i\int\frac{\mathrm{d}\omega}{2\pi}G^K_a G^A_b G^A_a G^A_b = 2\,\mathrm{Re}\,\mathrm{Lim}_{\delta\to 0}\,\mathrm{Res}_{G^R_a,\mathrm{pole}}\left(G^R_a G^A_b G^A_a G^A_b f_a(\omega)\right) \tag{D5b}$$

and for the causality-quenched configuration, accordingly:

$$\mathrm{Lim}_{\delta\to 0} 2i\int\frac{\mathrm{d}\omega}{2\pi}G^R_a G^R_b G^K_a G^A_b = 2\,\mathrm{Re}\,\mathrm{Lim}_{\delta\to 0}\Big[\mathrm{Res}_{G^A_a,\mathrm{pole}}\left(G^R_a G^R_b G^A_a G^A_b f_a(\omega)\right) + \mathrm{Res}_{G^R_b,\mathrm{pole}}\left(G^R_a G^R_b G^R_a G^A_b f_a(\omega)\right) - \mathrm{Res}_{G^A_b,\mathrm{pole}}\left(G^R_a G^R_b G^A_a G^A_b f_a(\omega)\right)\Big], \tag{D6a}$$

$$\mathrm{Lim}_{\delta\to 0} 2i \int \frac{\mathrm{d}\omega}{2\pi} G_a^R G_b^K G_a^A G_b^A = 2\,\mathrm{Re}\,\mathrm{Lim}_{\delta\to 0}\Big[\mathrm{Res}_{G_b^R,\mathrm{pole}}\left(G_a^R G_b^R G_a^A G_b^A f_b(\omega)\right) - \mathrm{Res}_{G_a^R,\mathrm{pole}}\left(G_a^R G_b^A G_a^A G_b^A f_b(\omega)\right) + \mathrm{Res}_{G_a^A,\mathrm{pole}}\left(G_a^R G_b^R G_a^A G_b^A f_b(\omega)\right)\Big], \quad \text{(D6b)}$$

which are derived using methods of contour integration as illustrated in Fig. 7.

As a consequence, we find the Ginzburg-Landau coefficients:

$$a_m = V_{\mathrm{SDW}} - 2\int (\mathrm{d}p)\,\frac{f_{\bar{1}} - f_1}{\xi_{\bar{1}} - \xi_1} \quad \text{(D7a)}$$

$$a_\Delta = V_{\mathrm{SC}} - \int (\mathrm{d}p) \sum_i \frac{f_i}{\xi_i} \quad \text{(D7b)}$$

$$u_m = -\int (\mathrm{d}p)\,\frac{2}{\left(\xi_{\bar{1}} - \xi_1\right)^2}\left[f'_{\bar{1}} + f'_1 - 2\,\frac{f_{\bar{1}} - f_1}{\xi_{\bar{1}} - \xi_1}\right] \quad \text{(D7c)}$$

$$u_\Delta = -\frac{1}{2}\int (\mathrm{d}p) \sum_i \frac{1}{\xi_i^2}\left[f'_i - \frac{f_i}{\xi_i}\right] \quad \text{(D7d)}$$

$$\gamma = \int (\mathrm{d}p)\frac{1}{\xi_{\bar{1}} - \xi_1}\left[\frac{f_{\bar{1}}}{\xi_{\bar{1}}^2} - \frac{f_1}{\xi_1^2} - \frac{f'_{\bar{1}}}{\xi_{\bar{1}}} + \frac{f'_1}{\xi_1}\right] \quad \text{(D7e)}$$

where we used $\bar{1} = -1$, $f_i = f(\xi_i)$, $f' = \partial_\xi f(\xi)$ and $\int (\mathrm{d}p) = \int \frac{d^2p}{4\pi^2}$. In equilibrium, where $f(\xi) = \tanh\left(\frac{\beta\xi}{2}\right)$, the expressions reduce to those derived in Ref. [39].

Because the two band dispersions are parametrized by $\xi_1 \equiv -\xi - b(\theta)$ and $\xi_{\bar{1}} = \xi$, with $b(\theta) = \delta_\mu + \delta_m \cos 2\theta$, the momentum integration can be split into an integration over momentum perpendicular to the FS (ξ) and momentum parallel to the FS (θ), $\int (\mathrm{d}p) = N_F \int \frac{\mathrm{d}\theta}{2\pi}\int \mathrm{d}\xi$, where N_F is the density of states. As a result, all the integrals over ξ can be performed analytically, leaving only the angular integrals to be evaluated numerically. In terms of the Fourier components of the anisotropic temperature δT_n, we find:

$$a_m = 4N_F\left(\ln\frac{T}{T_M} - \hat{a}_{m,\mathrm{eq}} + \sum_n \delta\hat{a}_{m,n}\frac{\delta T_n}{T}\right) \quad \text{(D8a)}$$

$$a_\Delta = 4N_F\left(\ln\frac{T}{T_c} + \sum_n \delta\hat{a}_{\Delta,n}\frac{\delta T_n}{T}\right) \quad \text{(D8b)}$$

$$u_m = \frac{N_F}{T^2}\left(\hat{u}_{m,\mathrm{eq}} + \sum_n \delta\hat{u}_{m,n}\frac{\delta T_n}{T}\right) \quad \text{(D8c)}$$

$$u_\Delta = \frac{N_F}{T^2}\left(\hat{u}_{\Delta,\mathrm{eq}} + \sum_n \delta\hat{u}_{\Delta,n}\frac{\delta T_n}{T}\right) \quad \text{(D8d)}$$

$$\gamma = \frac{N_F}{T^2}\left(\hat{\gamma}_{\mathrm{eq}} + \sum_n \delta\hat{\gamma}_n\frac{\delta T_n}{T}\right) \quad \text{(D8e)}$$

The equilibrium coefficients are given by:

$$\hat{a}_{m,\mathrm{eq}} = 2(\gamma_E + \ln 4) + \sum_{\alpha=\pm1}\left\langle\psi^{(0)}(X_\alpha)\right\rangle \quad \text{(D9a)}$$

$$\hat{u}_{m,\mathrm{eq}} = -\frac{1}{8\pi^2}\sum_{\alpha=\pm1}\left\langle\psi^{(2)}(X_\alpha)\right\rangle \quad \text{(D9b)}$$

$$\hat{u}_{\Delta,\mathrm{eq}} = \frac{7}{2\pi^2}\zeta(3) \quad \text{(D9c)}$$

$$\hat{\gamma}_{\mathrm{eq}} = \left\langle\frac{\psi^{(0)}\left(\frac{1}{2}\right)}{2\pi^2x^2}\right\rangle - \sum_{\alpha=\pm1}\left\langle\frac{\psi^{(0)}(X_\alpha) - i\alpha\frac{x}{\pi}\psi^{(1)}(X_\alpha)}{(2\pi x)^2}\right\rangle \quad \text{(D9d)}$$

where we introduced the notation $x = -\frac{\delta_\mu}{\pi T} - \frac{\delta_m}{\pi T}\cos 2\theta$ and $X_\alpha = \frac{1}{2} + \alpha i x$; the brackets denote integration over the angular variable and $\psi^{(n)}$ is the polygamma function of order n. The non-equilibrium coefficients are given by:

$$\delta\hat{a}_{m,n}(x) = 1 - \left\langle\frac{ix}{2}\sum_{\alpha=\pm1}\alpha\psi^{(1)}(X_\alpha)\,\cos n\theta\right\rangle \quad \text{(D10a)}$$

$$\delta\hat{a}_{\Delta,n} = \langle\cos n\theta\rangle = \delta_{n,0} \quad \text{(D10b)}$$

$$\delta\hat{u}_{m,n} = -\frac{1}{32\pi^2}\times \quad \text{(D10c)}$$

$$\times\sum_{\alpha=\pm1}\left\langle\left[\psi^{(2)}(X_\alpha) + \frac{\alpha i x}{2}\psi^{(3)}(X_\alpha)\right]\cos n\theta\right\rangle \quad \text{(D10d)}$$

$$\delta\hat{u}_{\Delta,n} = \frac{7}{2\pi^2}\zeta(3)\,\langle\cos n\theta\rangle = \frac{7}{2\pi^2}\zeta(3)\delta_{n,0} \quad \text{(D10e)}$$

$$\delta\hat{\gamma}_n = -\frac{1}{8\pi^2}\sum_{\alpha=\pm1}\left\langle\psi^{(2)}(X_\alpha)\,\cos n\theta\right\rangle \quad \text{(D10f)}$$

Note that, in the spirit of the Ginzburg-Landau approach, the temperature in the pre-factors of the quartic coefficients must be replaced by the temperature at which both transition lines meet, $T_M = T_c$. We verified that the equilibrium phase diagram resulting from these equations reproduce very well the transition lines of the phase diagram of Ref. [40] (including the T_M and T_c lines below, but in the vicinity of, the multicritical point), which used the full non-linear gap equations.